

## A study of long separation bubble on thick airfoils and its consequent effects



Amanullah Choudhry <sup>\*</sup>, Maziar Arjomandi, Richard Kelso

School of Mechanical Engineering, The University of Adelaide, South Australia 5005, Australia

### ARTICLE INFO

**Article history:**

Received 5 April 2014

Received in revised form 7 October 2014

Accepted 1 December 2014

**Keywords:**

Low Reynolds number

Camber effect

Airfoil transition modelling

Separation induced transition

Separation bubble

MAV

### ABSTRACT

A parametric study has been performed to analyse the flow around the thick-symmetric NACA 0021 airfoil in order to better understand the characteristics and effects of long separation bubbles (LoSBs) that exist on such airfoils at low Reynolds numbers and turbulence intensities. In the article, the prediction capabilities of two recently-developed transition models, the correlation-based  $\gamma$ - $Re_\theta$  model and the laminar-kinetic-energy-based  $\kappa$ - $\kappa_L$ - $\omega$  model are assessed. Two-dimensional steady-state simulations indicated that the  $\kappa$ - $\kappa_L$ - $\omega$  model predicted the separation and reattachment process accurately when compared with published experimental work. The model was then used to study the attributes and the effects of LoSBs as a function of the angle of attack, freestream turbulence intensity and Reynolds number. It was observed that LoSBs considerably degrade the aerodynamic performance of airfoils and lead to abrupt stall behaviour. It is, furthermore, illustrated that the presence of the LoSB leads to an induced camber effect on the airfoil that increases as the airfoil angle of attack increases due to the upstream migration of the bubble. An increase in the Reynolds number or turbulence levels leads to a reduction in the bubble extent, considerably improving the airfoil performance and leading to a progressive trailing-edge stall.

© 2014 Elsevier Inc. All rights reserved.

## 1. Introduction

Separation bubbles are generated primarily in applications involving low Reynolds number flows with large pressure gradients such as compressor blades in turbo-machines, high-altitude unmanned-air-vehicles, micro-air-vehicles and wind turbines (Lin and Pauley, 1996). The presence of the separation bubble is generally considered undesirable since it can impact the aerodynamic efficiency and stall behaviour of airfoils (Nakano et al., 2007; Zhang et al., 2008). The bubble can alter the flow at low Reynolds numbers and can consequently have adverse effects on the performance of the machine. Difficulties can also arise during airfoil testing in wind tunnels for applications involving high Reynolds number flows due to undesirable scale effects since most experimental wind tunnels operate in low Reynolds number regimes (Lissaman, 1983; Ol et al., 2005). The traditional methods to avoid these scale effects such as the addition of roughness strips and trip wires on airfoils or the addition of freestream turbulence also add a degree of complication and uncertainty to the process. Therefore,

the characteristics of the separation bubble and its effects need to be understood well to improve the design methodology of airfoils.

The most prevalent type of transition observed on airfoils and wings at low Reynolds numbers is the separation-induced transition. Separation-induced transition primarily occurs when a laminar boundary layer is exposed to large adverse pressure gradients, such as those near the leading edge of airfoils, resulting in its separation. The separated shear layer then undergoes transition due to amplification of velocity disturbances in the flow (Alam and Sandham, 2000a). The resulting turbulent shear layer reattaches some distance downstream resulting in the formation of an enclosed region commonly referred to as a separation bubble. The primary aspects of separation-induced transition, adapted from Horton (Horton, 1968), are illustrated in Fig. 1.

The location and size of the separation bubble is a function of the airfoil profile, freestream Reynolds number, turbulence intensity and the angle of attack (Tani, 1969; Swift, 2009). Separation bubbles can be classified either as short or long based on their chordwise extent and consequent effects on an airfoil pressure and velocity distributions. A short separation bubble (SSB) encompasses a chordwise extent of less than one percent and therefore does not influence the pressure distribution around the airfoil to a large degree (Tani, 1961). After transition occurs in the separated

\* Corresponding author at: School of Mechanical Engineering, The University of Adelaide, Adelaide, South Australia 5005, Australia. Tel.: +61 413032885.

E-mail address: [amanullah.choudhry@adelaide.edu.au](mailto:amanullah.choudhry@adelaide.edu.au) (A. Choudhry).

shear layer, the pressures start to return to the inviscid distribution that would exist if there was no bubble present (Katz and Plotkin, 1991). On the other hand, a long separation bubble (LoSB) can cover several percent of the airfoil chord and, therefore, severely affects the pressure distribution and the forces generated by the airfoil. Due to increased interaction with the exterior flow, the pressure distribution may be modified to such a large extent that it may be substantially different compared to the inviscid values (Gaster, 1966). The effects of both types can clearly be seen in Fig. 2 where it can be observed that the presence of the separation bubble results in a zero pressure gradient region due to flow stagnation inside the bubble (Gaster, 1969). Therefore, once the flow separates, the pressure barely changes due to the very low flow velocities and the relatively low streamline curvature in the free-stream flow. As shown by Bursnall and Loftin (1951), the flow is fully turbulent prior to reattachment, indicating that it is likely the transition process aids in the shear layer reattachment.

SSBs are commonly observed on thin airfoil sections near the leading edge where large pressure gradients exist and have been studied extensively (Crabtree, 1959; Von Doenhoff, 1938; Tani, 1939; Owen and Klanfer, 1953). It has been shown that an increase in the angle of attack or a reduction in the Reynolds number can lead to the ‘bursting’ of the bubble resulting in the formation of a LoSB or an unattached free shear layer (Gaster, 1969). Therefore, the LoSBs are considered as the precursor of thin airfoil stall (Bak et al., 1998). On the other hand, the effects of LoSBs have not been studied in much detail since it is believed that these exist only due to the bursting of SSBs. However, literature survey and experiments have revealed that long bubbles can exist on the suction side of thick airfoils at low Reynolds number and their presence dictates the aerodynamic efficiency and stall behaviour of thick airfoil sections (Jacobs, 1932; Raghunathan et al., 1988; Swalwell et al., 2001; Hansen et al., 2011). Therefore, it is important to understand the global characteristics of a long separation bubble in order to improve the understanding of its consequent effects on the performance of an airfoil at low Reynolds numbers. Such a study will aid in the selection of appropriate control techniques to avoid the possible losses incurred by the presence of LoSBs.

In aerospace applications, parametric studies are most conveniently performed using numerical modelling techniques. Efforts have been made by several researchers to understand the characteristics of laminar separation bubbles. Marxen et al. (2004) performed Direct Numerical Simulation (DNS) of flow over a flat plate in order to observe the basic characteristics of separation-induced transition. Galbraith and Visbal (2008) conducted Large Eddy Simulation (LES) in order to determine characteristics of the separation bubble on the SD7003 airfoil. However, the use of DNS and LES for wall-bounded flows requires prohibitively long runtimes and, therefore, these methods are not currently being used

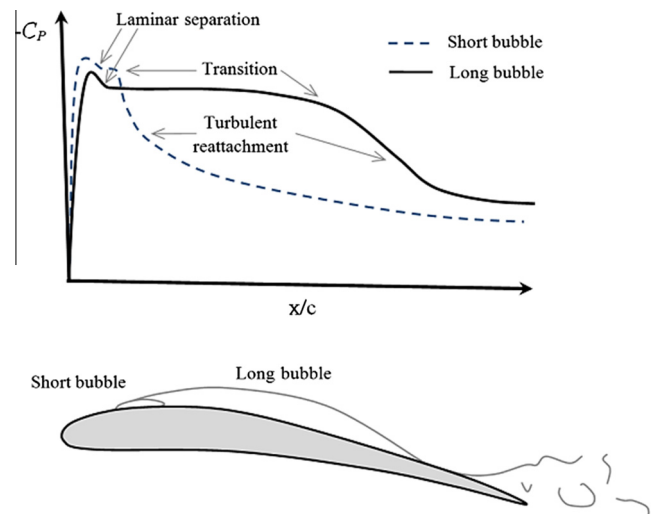


**Fig. 2.** The resultant pressure distribution on an airfoil due to presence of a short and long separation bubble.

for purposes other than research. On the other hand, RANS-based approaches coupled with linear-stability theory, offer an attractive alternative for prediction of separation-induced transition (Windte et al., 2006; Radespiel et al., 2007; Lian and Shy, 2007). In the present article, two recently-developed RANS-based transition models, the  $\gamma$ - $Re_\theta$  model (Menter et al., 2006) and the  $\kappa$ - $\kappa_L$ - $\omega$  model (Walters and Cokljat, 2008) have been tested and compared. Both models have been studied extensively against standard test cases and have been shown to predict the transition onset and extent with reasonable accuracy (Walters and Cokljat, 2008; Langtry et al., 2006; Menter, 2011). However, these RANS-based models have not been compared with each other before. The  $\gamma$ - $Re_\theta$  model has been shown to have superior prediction capabilities compared to other correlation-based models (Suluksa and Juntasaro, 2008). On the other hand, the  $\kappa$ - $\kappa_L$ - $\omega$  model focuses on the theory behind the model, instead of the results; however, there is little proof of the models' general applicability (Turner, 2012). Therefore, the two transition models have been assessed and compared in the current paper for the flow around NACA 0021 airfoil, based on the criteria established by Zingg and Godin (2009) for turbulence model assessment. In addition to this, a detailed analysis has been performed to study the characteristics of the LoSB and its effects on the performance of the NACA 0021 airfoil as a function of Reynolds number, freestream turbulence intensity and angle of attack. A peculiar effect of the LoSB has been noted in the present work and is discussed in detail in the article.

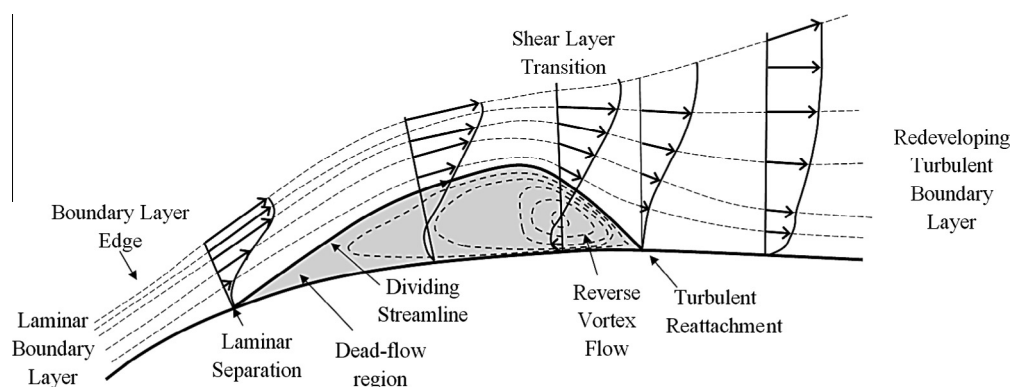


**Fig. 1.** Separation-induced transition, reproduced from Horton (1968).

## 2. Transition modelling

### 2.1. Correlation based intermittency model

The correlation-based intermittency model employing local variables,  $\gamma$ - $Re_\theta$  model, was first proposed in 2002 by Menter et al. (2002). Instead of using correlation-based functions to determine the transition onset, such as those proposed by Narasimha (1985) and Abu-Ghannam and Shaw (1980) the  $\gamma$ - $Re_\theta$  model was based on vorticity Reynolds number ( $Re_v$ ) which is dependent solely on local variables as shown:

$$Re_v = \frac{\rho y^2}{\mu} \frac{\partial u}{\partial y} = \frac{\rho y^2}{\mu} \Omega$$

Here  $\Omega$  is the vorticity and  $y$  is the wall normal distance. The maximum value of  $Re_v$  is dependent on the momentum thickness Reynolds number. The transport equation for intermittency is used to trigger the transition process and is given by Menter et al. (2006):

$$\frac{\partial \rho \gamma}{\partial t} + \frac{\partial \rho u_j \gamma}{\partial x_j} = P_{\gamma 1} - E_{\gamma 1} + P_{\gamma 2} - E_{\gamma 2} + \frac{\partial}{\partial x_j} \left[ \left( \mu + \frac{\mu_t}{\sigma_f} \right) \frac{\partial \gamma}{\partial x_j} \right]$$

The intermittency transport equation includes two proprietary functions:  $F_{length}$ , which controls the transition extent and  $Re_{\theta c}$  which determines the onset of transition. Furthermore, the transport equation for momentum thickness Reynolds number at the transition onset is given as:

$$\frac{\partial \rho Re_{\theta t}}{\partial t} + \frac{\partial \rho u_j Re_{\theta t}}{\partial x_j} = P_{\theta t} + \frac{\partial}{\partial x_j} \left[ \sigma_{\theta t} \left( \mu + \mu_t \right) \frac{\partial Re_{\theta t}}{\partial x_j} \right]$$

When the boundary layer separates, the transition model follows the following modification that allows the intermittency to exceed unity:

$$\gamma_{sep} = \min \left\{ 8 \max \left[ \left( \frac{Re_v}{2.193 Re_{\theta c}} \right) - 1, 0 \right] e^{-\left(\frac{R_T}{15}\right)^4}, 5 \right\} F_{\theta t}$$

Here,  $F_{\theta t}$  is the blending function that confines the modification to boundary layer type flows. The modification allows for larger production of turbulent kinetic energy at separation as well in order to hasten the reattachment. The artificial production of turbulence allows accurate modelling of turbomachinery applications for which the model was designed. The transition model has been coupled with Menter's  $\kappa-\omega$  SST model (Menter, 1994) where the production and destruction terms from the original SST model have been modified using the intermittency, making the  $\gamma$ - $Re_\theta$  model a four equation turbulence model. A complete description of the model is available in the article by Menter et al. (2006).

### 2.2. Laminar-kinetic-energy Model

The laminar-kinetic-energy model employed in the current article is the one proposed by Walters and Cokljat (2008) and is based on observations of the phenomena associated with laminar kinetic energy. Klebanoff (1971), while studying the effects of freestream turbulence on laminar boundary layers, discovered 'streaky structures' that lead to fluctuations in pressure and streamwise velocities. The fluctuation energy was termed as laminar kinetic energy. The laminar kinetic energy modelling can be coupled with existing turbulence models in order to improve the predictions of the transition process.

The (Walters and Cokljat, 2008)  $\kappa-\kappa_L-\omega$  model solves three additional transport equations for laminar and turbulent kinetic energy as well as the specific dissipation rate along with the basic RANS equations. The additional transport equations are:

$$\frac{D\kappa_T}{Dt} = P_{\kappa_T} + R_{BP} + R_{NAT} - \omega \kappa_T - D_T + \frac{\partial}{\partial x_j} \left[ \left( v + \frac{\alpha_T}{\sigma_\kappa} \right) \frac{\partial \kappa_T}{\partial x_j} \right]$$

$$\frac{D\kappa_L}{Dt} = P_{\kappa_L} - R_{BP} - R_{NAT} - D_L + \frac{\partial}{\partial x_j} \left[ v \frac{\partial \kappa_L}{\partial x_j} \right]$$

$$\begin{aligned} \frac{D\omega}{Dt} = & C_{\omega 1} \frac{\omega}{\kappa_T} P_{\kappa_T} + \left( \frac{C_{\omega R}}{f_W} - 1 \right) \frac{\omega}{\kappa_T} (R_{BP} + R_{NAT}) - C_{\omega 2} \omega^2 \\ & + C_{\omega 3} f_\omega \alpha_T f_W^{1/2} \frac{\kappa_T^{1/2}}{d^3} + \frac{\partial}{\partial x_j} \left[ \left( v + \frac{\alpha_T}{\sigma_\omega} \right) \frac{\partial \omega}{\partial x_j} \right] \end{aligned}$$

The terms in the model equations represent production, destruction and transport mechanisms. It should be noted that the model is  $\omega$ -based rather than being  $\varepsilon$ -based like the original version (Walters and Leylek, 2004) since it was observed that the  $\omega$ -based approach yields superior results in the transition onset predictions (Walters and Leylek, 2005).

The effects of the laminar and turbulent kinetic energy on the Reynolds stress terms was included through the total eddy viscosity concept (Volino, 1998), defined as:

$$\overline{-u_i' u_j'} = v_{TOT} \left( \frac{\partial u_i}{\partial x_j} + \frac{\partial u_j}{\partial x_i} \right) - \frac{2}{3} \kappa_{TOT} \delta_{ij}$$

Here,  $v_{TOT}$  is the sum of the small-scale eddy viscosity and the large scale eddy viscosity and  $\kappa_{TOT}$  is the sum of the turbulent and laminar kinetic energies. The laminar kinetic energy was used to describe the low frequency, high amplitude fluctuations in the pre-transitional laminar boundary layer. The fluctuations occur at a single scale and nearly all energy is contained in a single streamwise component. This implies that the process is largely two-dimensional and does not require a three-dimensional analysis. However, it is important to understand that these two-dimensional mechanisms are not equivalent to the instabilities caused by the 2D Tollmien–Schlichting (T-S) waves. Separation-induced transition can be considered as a type of bypass transition where the primary modes of natural transition, including the production of T-S waves, are 'by-passed' (Alam and Sandham, 2000b).

A complete description of the model equations and constants can be found in the articles by Walters and Leylek (2004) and Walters and Cokljat (2008).

## 3. Numerical method

### 3.1. Numerical scheme

The flow governing equations were solved using a cell-centred control volume space discretization approach for the fluid domain. The partial differential equations based on Reynolds Averaged Navier Stokes (RANS) equations are as follows:

$$\frac{\partial \rho}{\partial t} + \frac{\partial}{\partial x_i} (\rho u_i) = 0$$

$$\begin{aligned} \frac{\partial}{\partial t} (\rho u_i) + \frac{\partial}{\partial x_j} (\rho u_i u_j) = & - \frac{\partial p}{\partial x_i} + \frac{\partial}{\partial x_j} \left[ \mu \left( \frac{\partial u_j}{\partial x_i} + \frac{\partial u_i}{\partial x_j} - \frac{2}{3} \delta_{ij} \frac{\partial u_i}{\partial x_j} \right) \right] \\ & + \frac{\partial}{\partial x_j} (\rho \overline{u_i' u_j'}) \end{aligned}$$

The Reynolds stress term ( $\rho \overline{u_i' u_j'}$ ) is resolved using the turbulence model of choice to close the system of equations. In the present work, pressure–velocity coupling was handled using the implicit pressure-based algorithm SIMPLE. Steady-state simulations were performed which simplifies the above equations by eliminating the time marching. The choice of steady-state simulations was motivated by the seminal work of Pauley et al. (1990) who showed that LoSBs are steady separation bubbles without any vortex shedding. Simulations were initialized based on the

inlet boundary conditions. The equations were solved iteratively using second-order upwind scheme for spatial discretization of variables to improve the solution accuracy and numerical stability. The models were applied using the commercial software ANSYS® Fluent, Release 14.5. The lift and drag coefficients as well as the normalized residuals of all variables were monitored to ensure adequate convergence of the steady-state simulation.

The turbulence models were evaluated based on the criteria presented by Zingg and Godin (2009). The criteria and the relevant steps taken to ensure numerical accuracy are summarized as follows:

1. *Experimental flow conditions must be reproduced in the numerical work:* The experimental conditions of chord Reynolds number and freestream turbulence intensity were matched through a study conducted to determine the boundary conditions. The airfoil trailing edge was truncated at  $0.99c$  since zero thickness at the trailing edge is both practically unrealistic and problematic during grid-generation.
2. *Numerical error must be considerably smaller than the turbulence modelling errors:* This has been addressed by conducting a grid independence study to ensure adequate mesh resolution was achieved for the simulations.
3. *Experimental errors should be minimal:* Care was taken while selecting the appropriate experimental data sets based on accuracy. The data selected were the low Reynolds number experiments conducted on the NACA 0021 airfoil at the University of Adelaide KC wind tunnel (Hansen, 2012). Uncertainty analysis was performed to ensure that experimental predictions of forces and pressures were accurate. Further details can be found in the reference (Hansen, 2012).

4. *The location of laminar-turbulent transition must be known a priori and defined in the simulations:* The location of laminar separation and turbulent reattachment were deduced from the experimental pressure distributions. However, it is important to note that the location of transition was not defined in the present simulations in advance since this parameter was specifically being assessed.

### 3.2. Computational mesh

The computational grid employed in the present study for the simulation of flow around the NACA 0021 airfoil was constructed using POINTWISE® and is illustrated in Fig. 3. The mesh was constructed using an O-type grid topology, centred on the airfoil, in order to reduce the overall skewness of the near-wall elements as the mesh density is increased for the subsequent grid independence study. Structured quadrilateral elements were used in the current work since they provide the added advantage of a higher degree of control and accuracy, lower memory consumption and a faster convergence rate due to flow alignment with the grid elements (Sanders, 2009). A total of 250,000 elements were used to model the flow with 880 grid points along the airfoil surface and 284 in the wall-normal direction. The grid density was increased significantly as the mesh approached the airfoil from the boundaries to capture the salient flow features in the vicinity of the airfoil and to decrease the interpolation errors. The boundaries of the domain were placed at a distance of 20 chord lengths from the airfoil in order to ensure that the boundary location did not influence the flow (Fig. 3a). A total of 30 inflation layers were used in the vicinity of the airfoil to accurately model the boundary layer flow (Fig. 3b). The airfoil trailing edge was truncated in order to match the experiments (Fig. 3c). The height of the first cell was based on the required minimum value of  $y^+ \leq 1$  for the low-Re turbulent

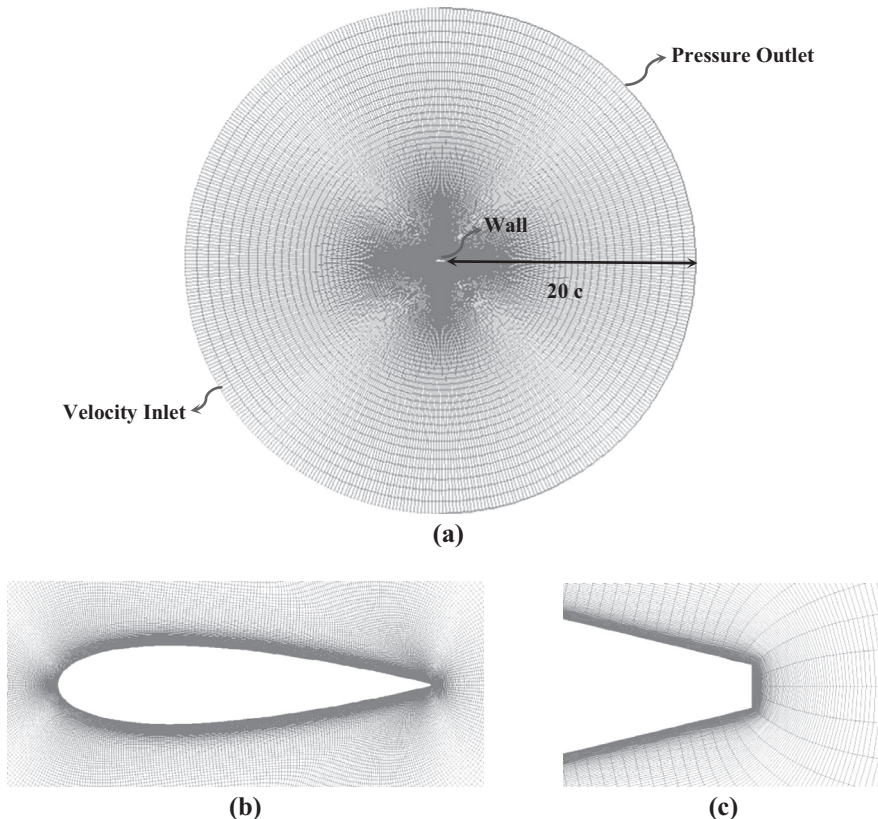


**Fig. 3.** (a) Typical grid topology used in the current study showing the overall grid resolution and boundary conditions. (b) Close-up view of the mesh in the vicinity of the airfoil. (c) Truncated trailing edge mesh.

models used in the current work in order to accurately model the boundary layer. Furthermore, the  $y^+$  was also checked as part of the routine post-processing for all simulations conducted in the present work and it was made certain to be less than one.

### 3.3. Boundary conditions

As can be observed in Fig. 3, the domain boundary was split into two regions, the velocity inlet and the pressure outlet, to implement the appropriate boundary conditions. The freestream velocity was specified at the inlet such that the chord Reynolds number of 120,000 was attained in the simulation to match the experiments. The angle of attack was also varied at the velocity inlet using the respective velocity components. The gauge pressure at the pressure outlet was specified to be zero. Furthermore, wall-condition ( $U = 0$ ) was specified for the airfoil surface so that the no-slip boundary condition was enforced and no turbulence was produced from the wall itself for both models. The freestream turbulence specification method chosen for the current work was to define the turbulence intensity and turbulence length scale at the inlet boundary. The inlet turbulence length scale and the inlet turbulence intensity are used in the Fluent CFD software to set the inlet specific dissipation rate and the turbulence kinetic energy respectively. These quantities are then calculated in the domain based on the transport equations presented earlier in Section 2. As suggested by Langtry and Menter (2005) for the  $\gamma$ - $Re_\theta$  model and by Walters and Cokljat (2008) for the  $\kappa$ - $k_L$ - $\omega$  model, the turbulent parameters at the inlet need to be specified such that the turbulence intensity in the vicinity of the body is similar to the experimental conditions. The turbulence intensity measured near the leading edge of the airfoil ( $TI_{LE}$ ) in the experiment was 0.6% (Hansen et al., 2011). Therefore, simulations were first conducted at an angle of attack of zero degrees in order to observe the effects of inlet turbulence length scale, the decay of turbulence intensity in the domain and to establish the appropriate turbulent parameters for the inlet boundary conditions. Since turbulence is a dissipative phenomenon, an arbitrarily large value of turbulence intensity of 7.5% was selected at the inlet and was kept constant while the inlet turbulence length scale was varied. As soon as the flow enters the domain, the turbulence is dissipated and the value of turbulence intensity rapidly falls as the flow progresses towards the leading edge of the airfoil. The final value of the turbulence intensity at the leading edge of the airfoil ( $TI_{LE}$ ) as a function of the inlet length scale at a Reynolds number of 120,000 is shown in Fig. 4 for both transition models. It can be observed that for similar turbulence length scales, the decay in turbulence intensities is more severe for the  $\kappa$ - $k_L$ - $\omega$  model. As stated earlier, the decay is governed by the transport equations of specific dissipation rate and turbulence

kinetic energy. Furthermore, note that the increase in the length scales associated with the turbulent structures results is a smaller decay rate of turbulence intensity. This makes intuitive sense since smaller structures are more prone to dissipation compared to larger eddies. Also indicated in the plot is the required turbulence intensity of the experiment (0.6%). Using this method, the appropriate boundary conditions for both transition models were obtained in order to satisfy the criterion set by Zingg and Godin (2009).

It should be noted here that the turbulence length scale does not play a significant role for this particular type of transition process. Here, the laminar boundary layer is expected to detach under the influence of adverse pressure gradients and then reattach after transitioning from laminar to turbulent flow. As shown by Butler et al. (2001) for a turbine blade cascade case where a similar transition process is observed, the process is not affected by the length scale of turbulent structures and is primarily dependent on the freestream turbulence intensity, Reynolds number and the pressure distribution. Similarly, experimental work by Cao (2010) demonstrated that the turbulence length scale had minimal effect on the performance of an airfoil at low freestream turbulence intensities and Reynolds numbers. The authors believe that the transition process is affected only when the length scales are comparable with the boundary layer thickness of the airfoil. However, in the present case and the works cited above, the length scales specified are at least order of magnitude smaller than the typical boundary layer thickness. Consequently, it is believed that the length scales, in this particular case, do not affect the transition process.

### 3.4. Grid independence study

A grid sensitivity analysis was performed to ascertain whether the selected grid density was of sufficient resolution and that the spatial discretization errors were minimal. The total number of elements of the original mesh was halved and doubled to generate two additional meshes for this study. The study was conducted at the angle of attack of zero and 4°, a Reynolds number of 120,000 and a  $TI_{LE}$  of 0.6%. The airfoil drag coefficient was monitored as the dependent variable for the study conducted at an angle of zero degrees whereas surface pressure distributions have been compared for the angle of attack of 4°. The dual check was performed in order to ensure that the mesh influence was locally small in the critical transitional flow region.

The results of the grid independence study are summarized in Table 1 where it can be observed that the mesh with 125,000 elements is sufficient, at a first glance. This is because doubling the mesh results in a little over 0.5% change in the predicted drag coefficient. However, comparison of the surface pressure distributions for the different mesh densities revealed instabilities in the predicted pressures on the airfoil suction side for the smaller mesh density of 125,000 elements. It is important to note that the instabilities were observed only for the  $\kappa$ - $k_L$ - $\omega$  model, as shown in Fig. 5(a), indicating that the chordwise resolution is not sufficient to capture the transition process. The instabilities disappeared as

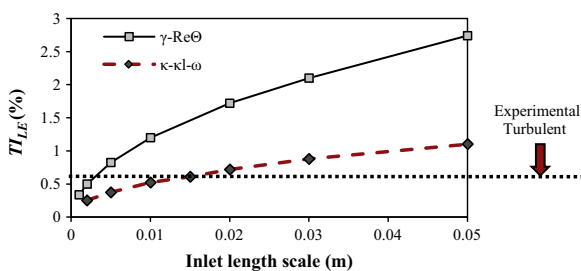


**Fig. 4.** Variation of turbulence intensity at the leading edge of the airfoil as a function of the specified inlet turbulence length scale for the two transition models. Note that the turbulence intensity specified at the inlet was kept constant at the arbitrary value of 7.5%. Therefore, the plot further indicates the decay rate of turbulence intensity as a function of the inlet length scales. The required turbulence intensity measured at the leading edge of the experiment is also indicated.

**Table 1**  
Grid independence study.

Mesh size (distribution)	Farfield location	$\gamma$ - $Re_\theta$	$\kappa$ - $k_L$ - $\omega$	Drag coefficient (0°)
125 k (440 × 284)	20c	0.01992496	0.026036741	
250 k (880 × 284)	20c	0.019799614	0.026192013	
500 k (1108 × 451)	20c	0.019696975	0.026138515	
				Drag coefficient (4°)
250 k (880 × 284)	20c	0.026083962	0.032757482	
344 k (880 × 391)	40c	0.026184851	0.032984562	

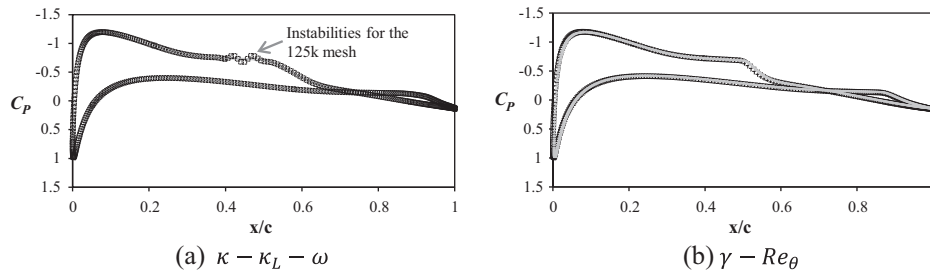


**Fig. 5.** Comparison of surface pressure distributions for two different mesh densities at an angle of attack of 4°. The smaller density mesh of 125,000 elements ( $\square$ ) exhibits instabilities in the surface pressure when compared with the larger mesh density of 250,000 elements (—) for the  $\kappa-\kappa_L-\omega$  model in (a). On the other hand, the pressure distribution is similar for the  $\gamma-Re_\theta$  model (b).

the mesh density was increased. On the other hand, for the  $\gamma-Re_\theta$  model, no such fluctuations in the surface pressures were observed for either mesh density, as shown in Fig. 5(b). A similar pressure distribution was observed for the largest mesh density of 500,000 elements for both models. Therefore, in order to ensure that the LoSB features were accurately modelled, the mesh size of 250,000 elements was found sufficient and hence used in subsequent studies.

A further study was conducted to ensure that the boundary location had a minimal effect on the airfoil performance. For this purpose, an additional mesh was generated with the same O-type grid topology centred on the airfoil. However, for this case, the far-field boundary was located at a distance of 40 chord lengths from the airfoil surface. A similar near-surface grid distribution was maintained in order to ensure that the solution was only sensitive to the farfield boundary location. Furthermore, the inlet boundary conditions were modified to ensure that the turbulence intensity was 0.6% near the airfoil leading edge. For this study, the drag coefficients were compared at a moderate angle of attack of 5°. The results have been summarized in Table 1 where it can be observed that the variation in drag coefficient as a result of the boundary location is negligible. Furthermore, apart from a slight increase in  $C_{p,\min}$ , the pressure distribution was also observed to be similar for both cases. Therefore, for the subsequent analysis, boundary location of 20c was considered sufficient.

### 3.5. Comparison of the transition models

The comparison of experimental and computed lift and drag coefficients is shown in Fig. 6. Simulations were conducted at a Reynolds number of 120,000 using the two transitional models over a range of angles to establish the accuracy of both models.

It can be observed that the  $\gamma-Re_\theta$  model under-predicts both lift and drag coefficients for most of the range of angles considered in the present study. The divergence of the coefficients increases

considerably as the angle of attack is increased. Even at the smaller angles, where complete flow separation is not observed, the values are under-predicted showing the inability of the  $\gamma-Re_\theta$  scheme to accurately model the aerodynamic characteristics influenced by the presence of the separation bubble. Furthermore, the  $\gamma-Re_\theta$  model, predicts a gradual stall behaviour more commonly observed on thick airfoil sections at high Reynolds number flows.

On the other hand, the  $\kappa-\kappa_L-\omega$  model shows a much better agreement with the experimental lift coefficient, specifically in the attached-flow regime. The deviation in the lift is still observed at the higher angles but to a lesser extent as compared to the  $\gamma-Re_\theta$  model. The drag coefficients, on the other hand, are exceedingly well-predicted by the  $\kappa-\kappa_L-\omega$  model, especially considering the two-dimensional nature of the simulations. Furthermore, the stall behaviour of the airfoil is modelled comparatively well through the  $\kappa-\kappa_L-\omega$  model. As can be observed, at such low Reynolds numbers the airfoil undergoes an abrupt stall, similar to thin airfoil sections, due to the bursting of the separation bubble.

A comparison of the measured and computed pressure coefficients at selected angles is shown in Fig. 7. In general, both models under-predict the suction pressures on the airfoil consistently, with the degree of discrepancy growing as the angle of attack is increased. The peak suction pressures on the airfoil upper surface are constantly under-predicted, as compared to the experiments, regardless of the angle of attack. On the other hand, the pressures on the lower side have been computed reasonably well, illustrating that the models can perform realistically for attached flows with negligible adverse pressure gradients.

It is interesting to note that both models tend to accurately capture the point of separation and transition to some extent for the cases where the flow is largely attached (Fig. 7a-d). These are the locations where the pressure distribution first levels off and where the pressure distribution starts to follow the ‘inviscid’ distribution, respectively as explained earlier. However, the  $\gamma-Re_\theta$  model predicts an earlier reattachment as compared to the  $\kappa-\kappa_L-\omega$  model

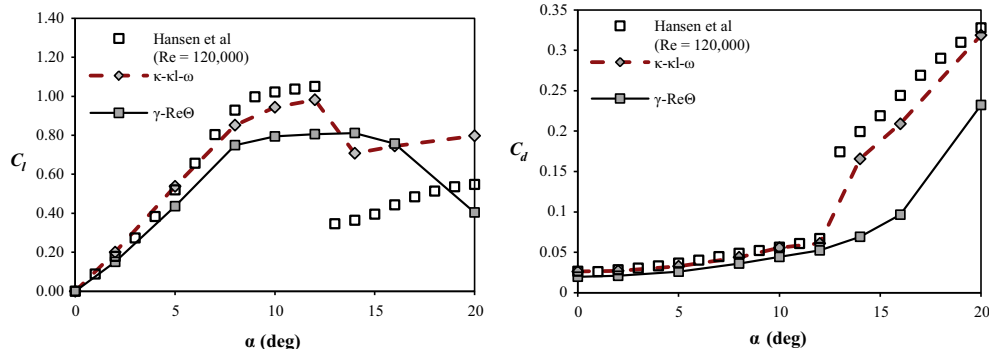


**Fig. 6.** Comparison of experimental and predicted force coefficients for the NACA 0021 airfoil at transitional Reynolds number of 120,000 using the two transition models.

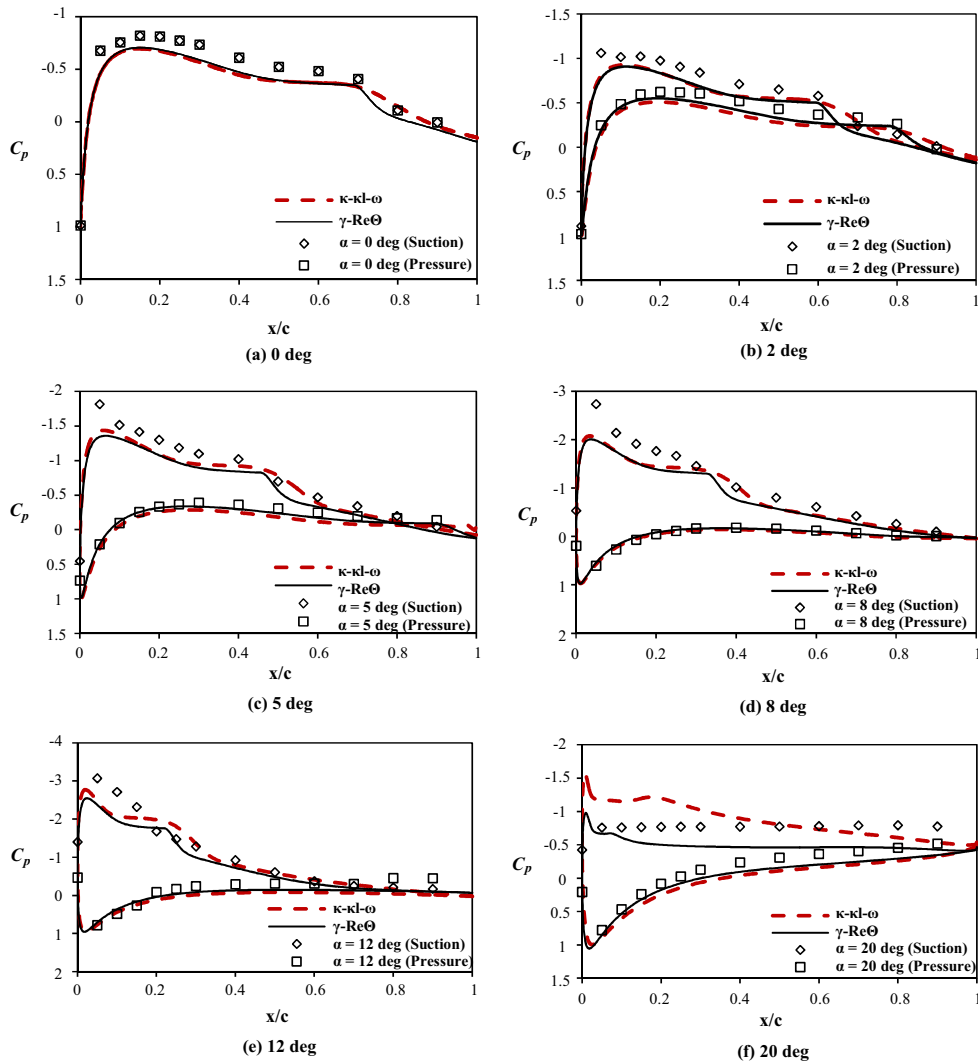


**Fig. 7.** Comparison of pressure coefficient distribution at selected angles of attack for the NACA 0021 airfoil at transitional Reynolds number of 120,000.

and the experiments. The inability to accurately predict the point of reattachment stems from the inherent empiricism employed in the model that allows additional turbulence to be generated as soon as the flow starts to transition (Menter et al., 2002; Langtry and Menter, 2005). This results in earlier reattachment of the flow as can be deduced from the pressure distributions presented in Fig. 7. On the other hand, the  $\kappa-\kappa_L-\omega$  model quite closely follows the experimental pressure distribution and accurately models the bubble behaviour, especially at the smaller angles. Furthermore, note that the minimum pressure coefficients as predicted by the two models are approximately similar, especially at the lower angles (Fig. 7a-d). Therefore, it is expected that the lift prediction should be at least comparable between the two models. However, as seen in Fig. 6, the lift predicted by the  $\gamma-Re_\theta$  model is smaller as compared to that predicted by the  $\kappa-\kappa_L-\omega$  model, even at lower angles of attack. The difference in the prediction of lift stems from the dissimilar pressure distributions computed by the two models associated with the separation bubble as shown in Fig. 7. The authors believe that the larger bubble predicted by the  $\kappa-\kappa_L-\omega$  model results in an induced camber effect on the airfoil due to alteration of the external flow. This induced camber effect due to the LoSB results in the increased and more accurate lift predictions by the  $\kappa-\kappa_L-\omega$  model.

The skin friction coefficient on the airfoil upper surface is illustrated in Fig. 8. Here, the predictions from the two models are compared at two representative angles. The distribution clearly depicts the location of laminar separation, turbulence onset, turbulent reattachment and turbulent separation, as predicted by the two models. The  $\kappa-\kappa_L-\omega$  model predicts a slightly earlier laminar separation and transition onset compared to the  $\gamma-Re_\theta$  model. However, notice that the 'strength' of the transition, the gradient of  $C_f$  curve after the transition onset, is more subtle for the  $\kappa-\kappa_L-\omega$  model. This leads to a delayed reattachment compared to that predicted by the  $\gamma-Re_\theta$  model and, therefore, a larger bubble is observed in this case. Note that as the angle of attack increases, the bubble starts to migrate upstream due to an earlier laminar separation caused by increased adverse pressure gradients.

The upstream migration of the LoSB on the airfoil surface as a function of increasing angle of attack is presented in Fig. 9. Here the velocity vectors of the mean-flow about the airfoil at selected angles of attack, calculated using the two turbulent models, are illustrated. Furthermore, the locations of laminar separation (LS), turbulent reattachment (TR) and the subsequent turbulent separation at higher angles are also illustrated. For the  $\kappa-\kappa_L-\omega$  model, it can be observed from Fig. 9 that at zero degrees, after laminar separation, the boundary layer does not reattach. On the other hand,

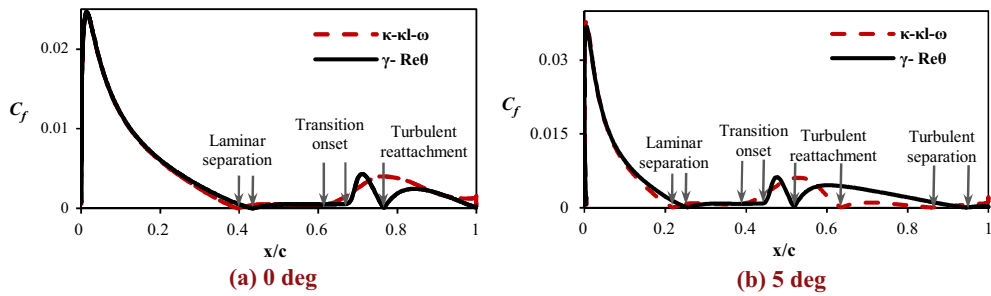


**Fig. 8.** Comparison of skin friction coefficient at the upper surface of the airfoil as predicted by the two transition models.

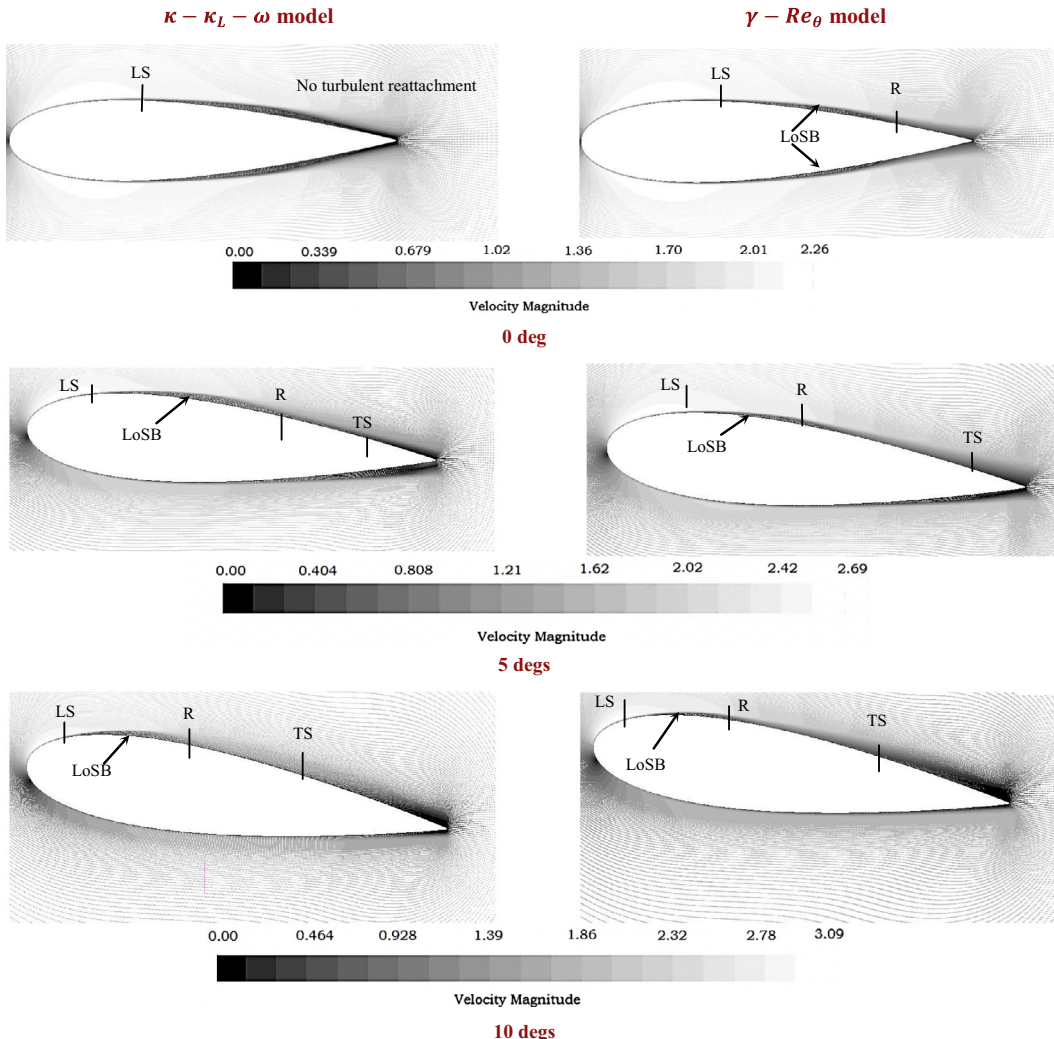


**Fig. 9.** Velocity vectors at selected incidences illustrating the LoSB on the NACA 0021 airfoil. The left column shows the vectors for the  $\kappa-\kappa_L-\omega$  model and the right column shows the same for the  $\gamma-Re_\theta$  model. The locations of laminar separation (LS) followed by turbulent reattachment (R) and the subsequent turbulent separation (TS) at higher angles are also marked for the upper surface of the airfoil.

for the  $\gamma-Re_\theta$  model, the separated shear layer reattaches near the trailing edge of the airfoil resulting in the formation of the LoSB even at the zero angle of incidence. This is primarily due to the artificial turbulence generated at the onset of turbulence, as stated earlier. As the angle of attack increases, the adverse pressure gradients increase near the leading edge of the airfoil causing earlier separation of the laminar boundary layer. The increased levels of turbulence at the higher angles aid in boundary layer transition, which leads to an earlier reattachment. Therefore, the bubble

length decreases as the bubble migrates upstream with the increase in the angle of attack.

A close-up view of the LoSB at an angle of attack of 10°, computed by the two models, is presented in Fig. 10 where the velocity vectors have been overlaid with the contours of turbulence intensity. Here, it can be observed quite clearly that the  $\kappa-\kappa_L-\omega$  model predicts a gradual increase in turbulence levels as the transition process begins, compared to the abrupt increase in the turbulence intensity predicted by  $\gamma-Re_\theta$  model. This abrupt increase

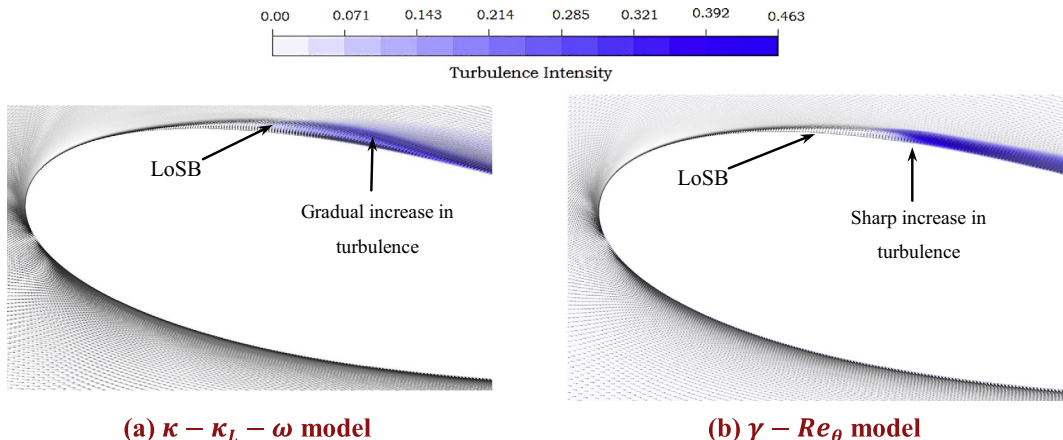


**Fig. 10.** A close-up view of the LoSB as computed by the two models on the NACA 0021 airfoil at an angle of attack of 10°. The height of the separated shear layer enclosing the LoSB can directly be observed here as being greater for the  $\kappa - \kappa_L - \omega$  model compared to the  $\gamma - Re_\theta$  model. Furthermore, the sharp rise in turbulence intensity is responsible for the rapid transition observed for the  $\gamma - Re_\theta$  model.

in the turbulence levels allows faster transition of the separated shear layer and hence leads to the earlier reattachment predicted by the  $\gamma - Re_\theta$  model, as explained before. Furthermore, due to the earlier reattachment, the height of the separated shear layer is visibly smaller as compared to height predicted by the  $\kappa - \kappa_L - \omega$  model. Therefore, the bubble thickness, computed by the  $\kappa - \kappa_L - \omega$  model, is also larger, leading to greater influence on the airfoil performance.

The separation of the laminar boundary layer, turbulent reattachment and the subsequent separation of the turbulent boundary layer have been determined using the wall shear stress, and reaffirmed using the surface pressure distributions on the airfoil. These are illustrated in Fig. 11 as a function of the angle of attack for both models. Here, it can clearly be observed that the  $\gamma - Re_\theta$  model predicts an earlier reattachment of the detached shear layer as compared to the  $\kappa - \kappa_L - \omega$  model leading to a smaller bubble extent. Furthermore, the  $\gamma - Re_\theta$  model predicts turbulent separation for an extended range of angles as compared to the  $\kappa - \kappa_L - \omega$  model. The artificial production of turbulence in the  $\gamma - Re_\theta$ , after laminar separation, results in a stronger turbulent boundary layer at reattachment. The outcome is higher mixing and exchange of momentum that leads to the prediction of a turbulent boundary layer that is comparatively less prone to re-separation, in comparison with the  $\kappa - \kappa_L - \omega$  model. This behaviour also causes the gradual stall prediction of the  $\gamma - Re_\theta$  model as compared to the  $\kappa - \kappa_L - \omega$  model which calculates a more accurate, abrupt stall behaviour of the airfoil at such conditions.

A direct visual to gauge the extent of the bubble predicted by the two models is illustrated in Fig. 12 where the length of the LoSB

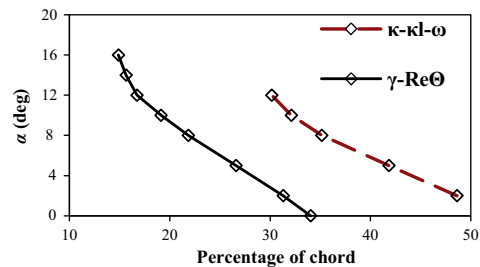


**Fig. 12.** Extent of the separation bubble predicted by the two models at a Reynolds number of 120,000 and  $T_{LE}$  of 0.6% as a function of the angle of attack.

is presented as a function of angle of attack. It can be observed that the  $\gamma - Re_\theta$  model predicts the separation bubble extent to be an average of 15% shorter compared to the  $\kappa - \kappa_L - \omega$  model. The bubble, therefore, does not affect the flow to such a high degree.

Based on these discussions, it can be inferred that the  $\kappa - \kappa_L - \omega$  model is superior in its predictions of the LoSB as compared to the  $\gamma - Re_\theta$  model. Therefore, in the subsequent analysis of the LoSB on a two-dimensional thick airfoil section, the  $\kappa - \kappa_L - \omega$  model is employed.

#### 4. The long separation bubble

##### 4.1. General characteristics

The general flow structure of a long separation bubble is similar to that of a short one apart from a few dissimilarities as shown in Fig. 13. The most prominent of these is that when, due to adverse pressure gradient, the laminar boundary layer separates, it spans a considerably larger distance prior to complete transition. The low entrainment rate of the dominantly laminar shear layer results in an extended region of trapped slow-moving or 'dead' flow. The extended dead flow region causes the zero pressure gradients observed in the pressure distributions around thick airfoils such as those shown in Fig. 7. As the downstream distance increases, the transition is initiated in the detached shear layer which results in increased entrainment and larger mixing. Further downstream, as the transition process completes, the detached shear layer starts to converge towards the airfoil surface resulting in a region of weak flow recirculation. The recirculating zone immediately after the dead air region is also of significant length compared to the ones observed in short bubbles. The detached shear layer is now effectively turbulent and leads to higher entrainment, larger Reynolds

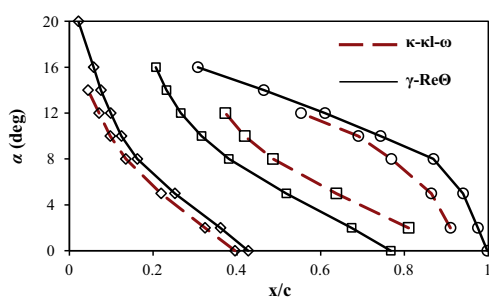


**Fig. 11.** Location of the laminar separation ( $\diamond$ ), turbulent reattachment ( $\square$ ) and turbulent separation ( $\circ$ ) points on the NACA 0021 airfoil at a Reynolds number of 120,000 and  $T_{LE}$  of 0.6% as a function of angle of attack.

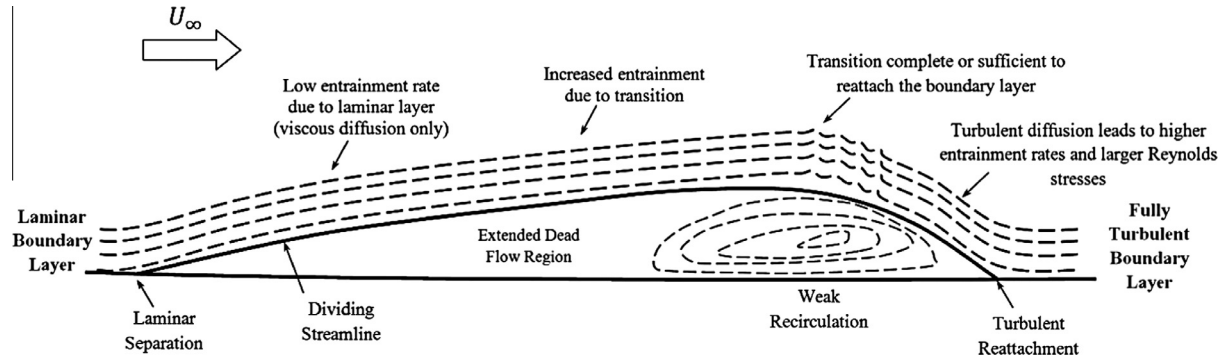


Fig. 13. General characteristics of a long separation bubble on a thick airfoil section.

stresses and streamline curvature as shown by Kelso et al. (1993). Finally, the detached shear layer attaches to the airfoil surface as a fully turbulent boundary layer resulting in the formation of the long separation bubble.

The long bubble, therefore, interacts with the external flow for a considerable length and alters the aerodynamic behaviour of the airfoil, primarily inducing a camber effect. A similar camber effect has been observed by the present authors in the works of Mueller and Batin (1982), Bastedo and Mueller (1986) and by Laitone (1997) for other thick airfoils operating at low Reynolds numbers. It can be observed from Fig. 11 that as the angle of attack increases, the bubble moves upstream due to earlier separation caused by the increased pressure gradients near the leading edge and earlier reattachment caused by the increased levels of disturbance at higher angles. As postulated by Von Doenhoff (1938), the separated flow proceeds tangent to the surface at the point of separation. Therefore, an increase in the angle of attack results in the increase in the separation angle of the shear layer resulting in the increase in the bubble thickness O'Meara and Mueller (1987) and hence the associated camber effect. Therefore, as the bubble moves towards the leading edge of the airfoil, the associated lift benefit increases since an airfoil with maximum camber point close to the leading edge produces higher lift (Hansen, 2012). However, it is important to note that the associated lift benefits are accompanied by drag penalties such that the overall lift-to-drag ratio is degraded due to the presence of the bubble. This is discussed further in the following sections.

#### 4.2. Effects of Reynolds number

Simulations were conducted to understand the global bubble behaviour as a function of the Reynolds number. The Reynolds number was varied while  $Tl_{LE}$  was kept constant at approximately

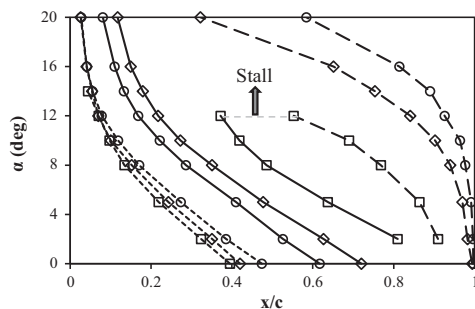


Fig. 14. Locations of the laminar separation (dotted), turbulent reattachment (solid) and turbulent separation (dashed) points at a constant  $Tl_{LE}$  of 0.61% as a function of Reynolds number ( $\square$  – 120,000,  $\diamond$  – 250,000,  $\circ$  – 500,000).

0.6%. As before, the separation of the laminar boundary layer, turbulent reattachment and the separation of the turbulent boundary layer were extracted using the wall shear stresses and pressure distributions on the airfoil. These are represented as the dotted, full and dashed lines respectively in Fig. 14. It can be observed that an increase in the Reynolds number results in significant changes in the overall bubble extent and the behaviour of the turbulent separation point. The following salient features can be observed:

- **Laminar separation:** As the Reynolds number increases, there is a delay in the laminar separation and the airfoil, therefore, experiences a larger laminar zone of reduced skin friction. However, at higher angles there is no noticeable influence of the Reynolds number on the laminar separation point.
- **Turbulent reattachment:** The increase in Reynolds number results in an accelerated transition process that causes earlier reattachment of the turbulent shear layer. Therefore, the turbulent reattachment point moves upstream as the Reynolds number is increased. This leads to a considerable reduction in the length of the separation bubble as the Reynolds number is increased.
- **Turbulent separation:** The increase in Reynolds number also tends to delay the separation of the turbulent boundary layer. This implies that the bubble itself has a little influence on the stall behaviour of the airfoil at larger Reynolds numbers.

Therefore, an increase in the Reynolds number substantially improves the airfoil performance in terms of a delay in stall and an increase in the maximum lift attainable.

A direct comparison of the lift-to-drag ratios and the extent of the bubble as a function of Reynolds number can be seen in Fig. 15. It can be observed that an increase in Reynolds number results in a significant decline in the extent of the separation bubble. As expected, an increase in the angle of attack further shrinks

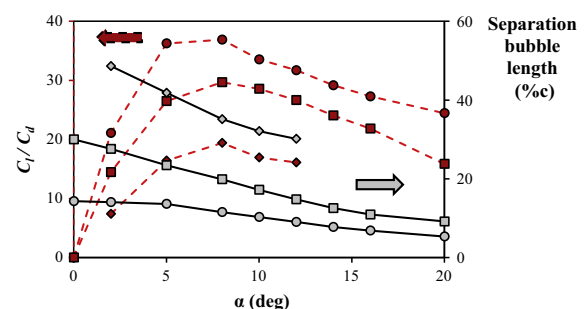


Fig. 15. Extent of the long separation bubble represented as a percentage of the chord length (solid lines) and consequent effect on the airfoil lift-to-drag ratio (dashed lines) as a function of Reynolds number ( $\diamond$  – 120,000,  $\square$  – 250,000,  $\circ$  – 500,000).

the bubble. At the highest Reynolds number of 500,000, there is an abrupt change in the length of the separation bubble observed from 5° to 8°. The increase in Reynolds number, therefore, leads to a substantial reduction in the bubble size and limits its negative influences on the airfoil. It is important to note however that it is not possible in the current case to isolate the effects of the bubble on the airfoil performance from the effects of the increasing Reynolds number. Therefore, a direct estimate of the effects of the bubble is only possible with a study of influence of turbulence intensity on the bubble as presented in the following section.

#### 4.3. Effects of turbulence intensity

Simulations were conducted at selected angles of attack from 0° to 20° in order to understand the effects of turbulence intensity on the global characteristics of the large separation bubble on the NACA 0021 airfoil at a Reynolds number of 120,000. The sensitivity of the bubble on the suction side of the airfoil as a function of  $Tl_{LE}$  are summarized in Fig. 16 where the laminar separation, turbulent reattachment and turbulent separation are shown as dotted, full and dashed lines respectively. The following salient features can be observed:

- *Laminar separation:* A delay in laminar separation occurs as the turbulence intensity is increased, resulting in a larger laminar zone. On the other hand, as the angle of attack increases, the laminar separation point moves upstream as expected for all cases. However, there is negligible effect of turbulence intensity on the laminar separation point location at high angles of attack.
- *Turbulent reattachment:* The turbulent reattachment point moves upstream as the turbulence intensity is increased, indicating that the transition process is considerably hastened due to the increase in the ambient turbulence intensity. This results in a comparatively smaller bubble on the suction side of the airfoil.
- *Turbulent separation:* The turbulent separation point moves downstream as the turbulence levels are increased resulting in delayed separation. On the other hand, as the angle of attack is increased, the turbulent separation point moves upstream under the influence of larger adverse pressure gradients.

The extent of the bubble and the consequent effects on the airfoil lift-to-drag ratio are illustrated in Fig. 17. It can be observed here that as the angle of attack increases, the size of the separation bubble decreases following an approximately similar pattern for all cases of  $Tl_{LE}$ . For the largest  $Tl_{LE}$  case, however, a slight abruptness in the extent of the separation bubble is observed, showing similar behaviour to the study of Bastedo and Mueller for the Wortmann

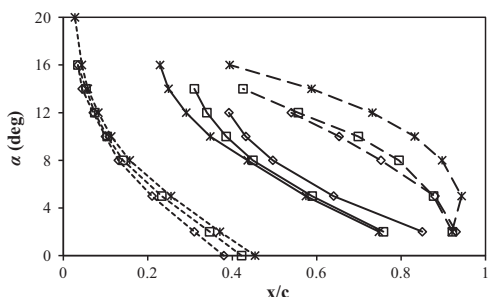


**Fig. 16.** Locations of laminar separation (dotted), turbulent reattachment (solid) and turbulent separation (dashed) points on the NACA 0021 airfoil at a Reynolds number of 120,000 as a function of  $Tl_{LE}$  ( $\diamond$  – 0.375%,  $\square$  – 1.1%,  $\times$  – 2.75%).

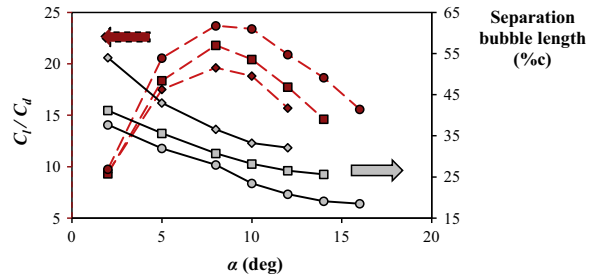


**Fig. 17.** Extent of the long separation bubble represented as a percentage of the chord length (solid lines) and consequent effect on the airfoil lift-to-drag ratio (dashed lines) as a function of  $Tl_{LE}$  ( $\diamond$  – 0.375%,  $\square$  – 1.1%,  $\circ$  – 2.75%).

FX63-137 airfoil (Bastedo and Mueller, 1986). The abrupt change in the extent occurs primarily due to the upstream movement of the turbulent reattachment point due to an increase in the accumulated ambient disturbances. However, unlike Bastedo and Mueller, we do not classify the bubble as a short separation bubble since it still encompasses a considerable portion of the airfoil chord.

The lift-to-drag ratio ( $C_l/C_d$ ) of the airfoil as a function of turbulence intensity is also presented in Fig. 17 in order to directly compare the effects of the bubble extent on the airfoil performance. It can be observed from the plot that the angle of maximum  $C_l/C_d$  is not influenced by the increase in the turbulence levels. However, a considerable improvement in the magnitude of maximum  $C_l/C_d$  can be observed as the extent of the bubble decreases. An approximate decrease in the bubble extent of 9% leads to an improvement of around 17% in the maximum  $C_l/C_d$ . The increase in ambient turbulence also results in an increase in the airfoil stall angle of attack. This primarily results from the greater mixing in the turbulent boundary layer which can then withstand the adverse pressures for larger extents.

A supplementary study was conducted at a Reynolds number of 120,000 in order to observe the airfoil performance without the presence of a separation bubble. In experiments, this can be accomplished by tripping the flow over the airfoil or by adding leading-edge roughness to make the boundary layer turbulent. However, in a numerical analysis, this would require significant re-meshing and re-modelling of the flow. Alternatively, the  $\gamma-Re_\theta$  model can be used to add roughness on the airfoil using user-defined-functions in the software. But, since the model has been deemed unsatisfactory for simulating the bubble behaviour, it has not been employed at this stage. Therefore, the  $\kappa-\kappa_L-\omega$  model was applied to simulate the flow at a sufficiently large turbulence intensity, in order to achieve a similar effect. The large increase in turbulence intensity at the leading edge of the airfoil aids in rapid transition of the attached flow, similar to the effects of distributed roughness strips. However, the drag in this case is expected to be higher compared to the imposed by-pass transition observed with roughness elements. For the supplementary study, a  $Tl_{LE}$  of 15% was found adequate to mitigate the presence of the bubble at all angles of attack.

Simulations at these conditions were conducted at the selected angles and the variation of lift-to-drag ratio as a function of angle of attack is presented in the Fig. 18. It can be noticed that, although the overall lift-to-drag ratio of the airfoil is reduced due to an increase in the turbulence intensity, there is a considerable improvement in the stall angle of attack. The lift-to-drag ratio is slightly degraded due to a large increase in the drag of the airfoil at such high turbulence levels. Furthermore, the camber effect associated with the bubble, described earlier, also disappears in this case due to the absence of the bubble. The increase in the airfoil stall angle of attack also occurs due to the turbulent boundary layer being more resistant to separation. Consequently, the airfoil

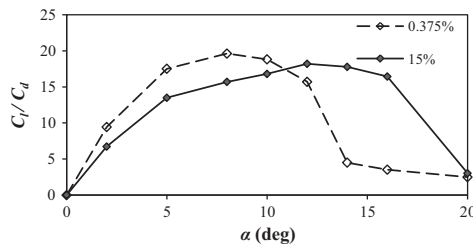


Fig. 18. Comparison of the airfoil performance at different  $T_{LE}$ .

does not undergo an abrupt stall due to the bursting of the bubble and instead experiences a progressive trailing edge stall. It can be observed that the mitigation of the bubble leads to an approximately 33% increase in the stall angle of attack.

Therefore, the decrease in the bubble extent considerably improves the performance of the airfoil by increasing the laminar zone, thus reducing the drag, and improving the overall lift-to-drag ratio due to a smaller bubble. The most practical benefit of a reduced bubble extent is the increase in the stall angle of attack. Therefore, for application involving low Reynolds numbers and turbulence intensities flows, such as MAVs and small wind turbines, the use of appropriate tripping techniques or the addition of roughness strips near the leading edge of thick airfoils would improve the performance, stability and operation of the device by diminishing the effects of the LoSB.

## 5. Conclusion

The flow around a two-dimensional NACA 0021 airfoil was calculated at low Reynolds numbers and turbulence intensities to study the long separation bubble and its effects on the airfoil performance. In the present article, two transition models, the correlation-based intermittency model developed by Menter et al. (2006) and the laminar-kinetic-energy model proposed by Walters and Cokljat (2008), were first evaluated based on the criteria established by Zingg and Godin (2009) for turbulence model assessment in order to ensure the accuracy and validity of the study presented in the article. Steady-state simulations of the airfoil were conducted in order to obtain the mean behaviour of the separation bubble and its effects on the airfoil performance. It was observed that both the  $\gamma$ - $Re_\theta$  model and the  $\kappa$ - $\kappa_L$ - $\omega$  model were able to predict the laminar boundary layer separation and the point of transition to some extent. However, due to the generation of additional turbulence, the  $\gamma$ - $Re_\theta$  model predicted earlier reattachment as compared to the  $\kappa$ - $\kappa_L$ - $\omega$  model and the experiments. This is primarily because the model has been calibrated for small separation bubbles observed in turbomachinery environments. The  $\gamma$ - $Re_\theta$  model relies heavily on empiricism and therefore suffers from a lack of universality. Therefore, the  $\kappa$ - $\kappa_L$ - $\omega$  model was deemed more suitable for studies related to the separation bubble on thick airfoil sections operating at low Reynolds numbers and small turbulence intensities.

Simulations were conducted using the  $\kappa$ - $\kappa_L$ - $\omega$  model at several turbulence levels and Reynolds numbers to study the characteristics of the long separation bubble and its effects on the NACA 0021 airfoil over a range of angles. The global features of the long separation bubble were studied by evaluating the locations of the points of laminar separation and turbulent reattachment. It was observed that the extent of the bubble decreases as the angle of attack, Reynolds number or freestream turbulence levels are increased. The bubble, due to its significant extent, had a profound impact on the performance of the airfoil. Of particular note is the induced camber effect on the airfoil that leads to a higher lift generation, but with the cost of increased drag. The overall lift-to-drag

ratio of the airfoil, therefore, was degraded due to the presence of the bubble. An increase in the Reynolds number or the turbulence intensity resulted in the decrease of the bubble extent, thereby considerably improving the performance of the airfoil. The presence of the bubble and alteration of flow in the immediate vicinity of the airfoil can also be translated to similar effects observed on pitching airfoils undergoing dynamic stall. In this case, the large-scale vorticity can lead to changes in the camber and thickness of airfoils and, therefore, cause the non-linearity observed in the airfoil lift during the pitching cycle (Choudhry et al., 2014).

The present study demonstrates that large separation bubbles degrade the performance of airfoils to a significant extent by decreasing the overall lift-to-drag ratio and incurring abrupt stall. It was observed that an approximate decrease in the bubble extent of 9% leads to an improvement in the lift-to-drag ratio of about 17%. Furthermore, the complete mitigation of the bubble, due to increase of turbulence levels, resulted in the increase of the stall angle of attack by approximately 33%. This confirms the need for the addition of roughness elements or tripping devices near the leading edges of thick airfoil sections for application involving low Reynolds numbers and turbulence intensities flows such as those encountered in MAVs and small wind turbines. Such a measure will improve the performance and stability of the airfoil by reducing the effects of the LoSB on the thick airfoil and significantly improve the operation of the device.

## References

- Abu-Ghannam, B., Shaw, R., 1980. Natural transition of boundary layers—the effects of turbulence, pressure gradient, and flow history. *J. Mech. Eng. Sci.* 22, 213–228.
- Alam, M., Sandham, N., 2000a. Direct numerical simulation of 'short' laminar separation bubbles with turbulent reattachment. *J. Fluid Mech.* 410, 1–28.
- Alam, M., Sandham, N.D., 2000b. Direct numerical simulation of 'short' laminar separation bubbles with turbulent reattachment. *J. Fluid Mech.* 403, 223–250.
- Bak, C., Aagaard Madsen, H., Fuglsang, P., Rasmussen, F., 1998. Double stall.
- Bastedo, W.G., Mueller, T., 1986. Spanwise variation of laminar separation bubbles on wings at low Reynolds number. *J. Aircraft.* 23, 687–694.
- Burnsall, W.J., Loftin, L.K., 1951. Experimental investigation of localized regions of laminar-boundary-layer separation. National Advisory Committee for Aeronautics.
- Butler, R.J., Byerley, A.R., VanTreuren, K., Baughn, J.W., 2001. The effect of turbulence intensity and length scale on low-pressure turbine blade aerodynamics. *Int. J. Heat Fluid Flow* 22, 123–133.
- Cao, N., 2010. Effects of turbulence intensity and integral length scale on an asymmetric airfoil at low Reynolds numbers.
- Choudhry, A., Leknys, R., Arjomandi, M., Kelso, R., 2014. An insight into the dynamic stall lift characteristics. *Exp. Thermal Fluid Sci.* 58, 188–208.
- Crabtree, L., 1959. The Formation of Regions of Separated Flow on Wing Surfaces. HM Stationery Office.
- Galbraith, M., Visbal, M., 2008. Implicit large eddy simulation of low Reynolds number flow past the SD7003 airfoil. *AIAA Paper 225*, 2008.
- Gaster, M., 1966. Structure and behavior of laminar separation bubbles. *AGARD CP 4*, 813–854.
- Gaster, M., 1969. The Structure and Behaviour of Laminar Separation Bubbles. HM Stationery Office.
- Hansen, K.L., 2012. Effect of leading edge tubercles on airfoil performance.
- Hansen, K.L., Kelso, R.M., Dally, B.B., 2011. Performance variations of leading-edge tubercles for distinct airfoil profiles. *AIAA J.* 49, 185–194.
- Horton HP. Laminar separation bubbles in two and three dimensional incompressible flow, 1968.
- Jacobs, E.N., 1932. The Aerodynamic Characteristics of Eight Very Thick Airfoils from Tests in the Variable Density Wind Tunnel. National Advisory Committee for Aeronautics.
- Katz, J., Plotkin, A., 1991. Low-Speed Aerodynamics: from Wing Theory to Panel Methods. McGraw-Hill, Singapore.
- Kelso, R., Lim, T., Perry, A., 1993. The effect of forcing on the time-averaged structure of the flow past a surface-mounted bluff plate. *J. Wind Eng. Ind. Aerodyn.* 49, 217–226.
- Klebanoff, P., 1971. Effect of free-stream turbulence on the laminar boundary layer. *Bull. Am. Phys. Soc.* 10, 1323.
- Laitone, E., 1997. Wind tunnel tests of wings at Reynolds numbers below 70 000. *Exp. Fluids* 23, 405–409.
- Langtry, R., Menter, F., 2005. Transition modeling for general CFD applications in aeronautics. *AIAA Paper 522*, 2005.
- Langtry, R.B., Menter, F., Likki, S., Suzen, Y., Huang, P., Völker, S., 2006. A correlation-based transition model using local variables—Part II: test cases and industrial applications. *J. Turbomach.* 128, 423–434.

- Lian, Y., Shyy, W., 2007. Laminar-turbulent transition of a low Reynolds number rigid or flexible airfoil. *AIAA J.* 45, 1501–1513.
- Lin, J.M., Pauley, L.L., 1996. Low-Reynolds-number separation on an airfoil. *AIAA J.* 34, 1570–1577.
- Lissaman, P., 1983. Low-Reynolds-number airfoils. *Annu. Rev. Fluid Mech.* 15, 223–239.
- Marxen, O., Rist, U., Wagner, S., 2004. Effect of spanwise-modulated disturbances on transition in a separated boundary layer. *AIAA J.* 42, 937–944.
- Menter, F.R., 1994. Two-equation eddy-viscosity turbulence models for engineering applications. *AIAA J.* 32, 1598–1605.
- Menter, F.R., 2011. Turbulence Modeling for Engineering Flows. ANSYS Inc.
- Menter, F., Esch, T., Kubacki, S. Transition modelling based on local variables. In: Proceedings of the 5th International Symposium on Engineering Turbulence Modeling and Measurements, 2002.
- Menter, F., Langtry, R., Likki, S., Suzen, Y., Huang, P., Völker, S., 2006. A correlation-based transition model using local variables-Part I: model formulation. *J. Turbomach.* 128, 413–422.
- Mueller, T.J., Battil, S.M., 1982. Experimental studies of separation on a two-dimensional airfoil at low Reynolds numbers. *AIAA J.* 20, 457–463.
- Nakano, T., Fujisawa, N., Oguma, Y., Takagi, Y., Lee, S., 2007. Experimental study on flow and noise characteristics of NACA0018 airfoil. *J. Wind Eng. Ind. Aerodyn.* 95, 511–531.
- Narasimha, R., 1985. The laminar-turbulent transition zone in the boundary layer. *Prog. Aerosp. Sci.* 22, 29–80.
- OI, M.V., McAuliffe, B.R., Hanff, E.S., Scholz, U., Kähler, C., 2005. Comparison of laminar separation bubble measurements on a low Reynolds number airfoil in three facilities. *AIAA Paper 5149*, 2005.
- O'Meara, M., Mueller, T., 1987. Laminar separation bubble characteristics on an airfoil at low Reynolds numbers. *AIAA J.* 25, 1033–1041.
- Owen, P., Klanfer, L., 1953. On the laminar boundary layer separation from the leading edge of a thin aerofoil. Defense Tech. Inform. Center.
- Pauley, L.L., Moin, P., Reynolds, W.C., 1990. The structure of two-dimensional separation. *J. Fluid Mech.* 220, 397–411.
- Radespiel, R.E., Windte, J., Scholz, U., 2007. Numerical and experimental flow analysis of moving airfoils with laminar separation bubbles. *AIAA J.* 45, 1346–1356.
- Raghunathan, S., Harrison, J., Hawkins, B., 1988. Thick airfoil at low Reynolds number and high incidence. *J. Aircraft.* 25, 669–671.
- Sanders, D.D., 2009. CFD Modeling of Separation and Transitional Flow in Low Pressure Turbine Blades at Low Reynolds Numbers. Virginia Polytechnic Institute and State University.
- Suluksna, K., Juntasaro, E., 2008. Assessment of intermittency transport equations for modeling transition in boundary layers subjected to freestream turbulence. *Int. J. Heat Fluid Flow* 29, 48–61.
- Swalwell, K., Sheridan, J., Melbourne, W., 2001. The effect of turbulence intensity on stall of the NACA 0021 aerofoil. In: Proceedings 14th Australasian Fluids Mechanics Conference. Adelaide University, p. 941–944.
- Swift, K.M., 2009. An Experimental Analysis of the Laminar Separation Bubble at Low Reynolds Numbers.
- Tani, I., 1939. Note on the interplay between the laminar separation and the transition from laminar to turbulent of the boundary layer (In Japanese). *J. Soc. Aero. Sci. Japan* 6, 122–134.
- Tani, I., 1961. Critical Survey of Published Theories on the Mechanism of Leading-Edge Stall. Aeronautical Research Institute.
- Tani, I., 1969. Boundary-layer transition. *Annu. Rev. Fluid Mech.* 1, 169–196.
- Turner, C., 2012. Laminar Kinetic Energy Modelling for Improved Laminar-Turbulent Transition Prediction. The University of Manchester.
- Volino, R., 1998. A new model for free-stream turbulence effects on boundary layers. *J. Turbomach.* 120, 613–620.
- Von Doenhoff, A.E., 1938. A Preliminary Investigation of Boundary-Layer Transition Along a Flat Plate With Adverse Pressure Gradient. National Advisory Committee for Aeronautics.
- Walters, D.K., Cokljat, D., 2008. A three-equation eddy-viscosity model for Reynolds-averaged Navier-Stokes simulations of transitional flow. *J. Fluids Eng.* 130, 121401.
- Walters, D.K., Leylek, J.H., 2004. A new model for boundary layer transition using a single-point RANS approach. *Trans. ASME-T-J. Turbomachinery* 126, 193–202.
- Walters, D.K., Leylek, J.H., 2005. Computational fluid dynamics study of wake-induced transition on a compressor-like flat plate. *J. Turbomach.* 127, 52–63.
- Windte, J., Scholz, U., Radespiel, R., 2006. Validation of the RANS-simulation of laminar separation bubbles on airfoils. *Aerosp. Sci. Technol.* 10, 484–494.
- Zhang, W., Hain, R., Kähler, C.J., 2008. Scanning PIV investigation of the laminar separation bubble on a SD7003 airfoil. *Exp. Fluids* 45, 725–743.
- Zingg, D., Godin, P., 2009. A perspective on turbulence models for aerodynamic flows. *Int. J. Comput. Fluid Dynam.* 23, 327–335.